The Impact of Microstructure on Filament Growth at the Sodium Metal Anode in All-Solid-State Sodium Batteries

Ziming Ding, Yushu Tang, Till Ortmann, Janis Kevin Eckhardt, Yuting Dai, Marcus Rohnke, Georgian Melinte, Christian Heiliger, Jürgen Janek, and Christian Kübel*

In recent years, all-solid-state batteries (ASSBs) with metal anodes have witnessed significant developments due to their high energy and power density as well as their excellent safety record. While intergranular dendritic lithium growth in inorganic solid electrolytes (SEs) has been extensively studied for lithium ASSBs, comparable knowledge is missing for sodium-based ASSBs. Therefore, polycrystalline Na-β''-alumina is employed as a SE model material to investigate the microstructural influence on sodium filament growth during deposition of sodium metal at the anode. The research focuses on the relationship between the microstructure, in particular grain boundary (GB) type and orientation, sodium filament growth, and sodium ion transport, utilizing in situ transmission electron microscopy (TEM) measurements in combination with crystal orientation analysis. The effect of the anisotropic sodium ion transport at/across GBs depending on the orientation of the sodium ion transport planes and the applied electric field on the current distribution and the position of sodium filament growth is explored. The in situ TEM analysis is validated by large field of view post-mortem secondary ion mass spectrometer (SIMS) analysis, in which sodium filament growth within voids and along grain boundaries is observed, contributing to the sodium network formation potentially leading to failure of batteries.

1. Introduction

ASSBs with metal anodes (e.g., Li and Na) are projected to show high energy and power density and overcome the safety limitations of their liquid electrolyte counterparts (lithium-ion batteries, sodium-ion batteries). The key component of ASSBs is the SE, and its interface with the electrode materials is crucial for the cell stability and kinetics. The emergence of sodium SEs traces its origins to a significant milestone in battery development, namely the pioneering discovery of swift two-dimensional Na$^+$ ion diffusion within beta-alumina (Na$_2$O-11Al$_2$O$_3$) compounds in the 1930s.[1,2] This breakthrough, made as early as the 1960s, quickly found practical application in the form of high-temperature Na–S batteries[3] and later in the 1980s, in Na–NiCl$_2$ batteries,[4] establishing a strong foundation for the advancement of sodium SE technologies. However, few commercial ASSBs working at room temperature have been reported, as the performances of ASSBs are strongly restrained by the sluggish kinetics at room temperature and solid-solid interfacial problems.[5] Among various interfacial problems, metal filamentary growth-induced cell failure cannot yet be avoided as initially expected for ASSBs despite the high elastic modulus of SEs compared to liquid electrolytes.[5] With the strong trend toward high-energy cells with lithium metal anode, a series of comprehensive

Z. Ding, Y. Tang, Y. Dai, G. Melinte, C. Kübel
Institute of Nanotechnology (INT) and Helmholtz Institute Ulm (HIU)
Karlsruhe Institute of Technology (KIT)
76344 Eggenstein-Leopoldshafen, Germany
E-mail: Christian.kuebel@kit.edu
Z. Ding, C. Kübel
Technische Universität Darmstadt
64289 Darmstadt, Germany

T. Ortmann, J. K. Eckhardt, M. Rohnke, C. Heiliger, J. Janek
Institute for Physical Chemistry
Justus Liebig University Giessen
35392 Giessen, Germany
T. Ortmann, J. K. Eckhardt, M. Rohnke, C. Heiliger, J. Janek
Center for Materials Research (ZfM)
Justus Liebig University Giessen
35392 Giessen, Germany
J. K. Eckhardt, C. Heiliger
Institute for Theoretical Physics
Justus Liebig University Giessen
35392 Giessen, Germany
C. Kübel
Karlsruhe Nano Micro Facility (KNMF)
Karlsruhe Institute of Technology (KIT)
76344 Eggenstein-Leopoldshafen, Germany

**ADVANCED
SCIENCE NEWS**

www.advancedsciencenews.com

**ADVANCED
ENERGY
MATERIALS**

www.advenergymat.de

studies of Li filament growth mechanisms have been conducted. In contrast to the directional dendrite growth in liquid electrolytes, studies reported dispersed filamentary Li dendrites to nucleate at the Li/SEs interface and inside SEs (e.g., at voids and GBs) penetrating along GBs and even across grains of the SE towards the cathode.[6–9] Moreover, the Li penetration is strongly dependent on the SE composition (e.g., LiPON-, $Li_7La_3Zr_2O_{12}$-(LLZO-) and Li_2S-P_2S_5-based, etc.).[10,11] Unlike glassy sulfide or polymer-based SEs, most oxide-based electrolytes exhibit a polycrystalline nature, in which the GBs are one of the non-negligible microstructural constituents that strongly influence Li-ion transport and filament growth. For instance, it is widely accepted that GBs have a higher resistance for ion migration across them due to the structural mismatch between adjacent grains and the complex/disordered GB core.[12] Moreover, for selected GBs in LLZO it has been shown that they exhibit a lower shear modulus[13] and bandgap[8] contributing to Li nucleation and penetration.

Despite these impediments created by GBs for high-performance ASSBs, GBs can also provide a fast Li-ion transport path along GBs due to the enhanced free volume at GBs, typically in poorly conducting SEs.[14,15] In addition, Wang et al. discovered that ions diffusing along GBs show a lower energy barrier than across GBs in cubic Na_3PS_4 by first principle and phase field calculations.[16] Besides the anisotropic effects of GBs on ion diffusion, anisotropic Na^+ ion migration occurs within the grain bulk of layered SE or SE with channel-like ion paths. Examples include the well-known Na superionic conductor (Na-SICON) ($Na_3Zr_2Si_2PO_{12}$), which exhibits anisotropic transport in 3D,[17] and Na-β''-alumina with its layered crystal structure, which results in a 2D transport path. However, the impact of these distinctive microstructural properties on the Na filament growth during Na deposition has not been investigated in any detail.

The oxide-based solid sodium electrolytes such as $Na_{3.4}Zr_2Si_{2.4}P_{0.6}O_{12}$ and Na-β''-alumina have been explored recently as a promising candidate for room temperature ASSBs due to their stability against the Na metal anode and high ionic conductivity.[18,19] Therefore, they might be suitable for fast-charging solid-state battery cells.[19,20] Hence, in order to understand the influence of the microstructure and especially the anisotropic ion transport on Na filament growth during Na deposition, we built a Na-β''-alumina-based model system to observe the cathodic sodium deposition inside a TEM. The in situ TEM measurements were correlated with local crystal orientation analysis as the basis for corresponding computational transport simulations to investigate the relationship between the microstructure and Na filament growth as well as Na^+ ion transport. This work is complemented by postmortem secondary ion mass spectrometry (SIMS) analysis to analyze microstructural features (e.g., voids, filament growth) at a larger scale to establish a complete microstructural model.

2. Results and Discussion

2.1. In Situ Transmission Electron Microscopy (TEM) Observation of Na Filament Formation

To understand the impact of the microstructure of polycrystalline Na-β''-alumina on the Na^+ ion transport and Na filament growth

at room temperature, we employed the in situ biasing setup shown in **Figure 1**a and Figure S1a (Supporting Information). The W tip was positioned with high precision to contact the Na-β''-alumina directly as shown in Figure 1b–e and Figure S1 (Supporting Information) and a bias was applied to drive the Na^+ ion migration. The thick Na-β''-alumina frame connected to the Cu grid was reduced[21,22] and acted as a Na source in this experiment. The hypothesis was that Na plating would occur in the vicinity of the local electric contact between the W tip and the Na-β''-alumina grain due to charge transfer by electrons from the W tip at the contact area. Indeed, Na plating occurred in this region after biasing as shown by scanning transmission electron microscopy energy dispersive X-ray spectroscopy (STEM-EDX) elemental mapping in Figure S1d (Supporting Information). However, during biasing filamentary sodium growth started at the GB as indicated by the green arrows in Figure 1b–e. The growth at this GB was more dominant than at the interface with the W tip. This behavior suggests that Na deposition is strongly affected by the microstructure and, in particular, GBs appear to be preferred regions for Na filament growth inside Na-β''-alumina.

Since the setup in Figure S1a (Supporting Information) with a direct local electric contact between the W tip and a Na-β''-alumina grain results in a highly non-uniform electric field distribution, this renders a larger scale analysis of the relationship between the microstructure and the Na^+ ion transport and Na plating difficult. Therefore, we built a Na-β''-alumina│Au(Pt) system to provide a uniform potential to all grains next to the Au(Pt) electrode as shown in Figure 1a. Using the setup, we investigated the Na metal distribution and crystal structure evolution during the Na filament formation as shown in **Figure 2** and Figure S2 (Supporting Information). During biasing, the Na filaments appeared at the GB between the grains denoted as G1 and G2 as well as at the Au(Pt) electrode as shown in Figure 2c. They were identified as Na based on the EDX Na map (Figure 2d). The appearance of the peak at around 6 eV in the low loss electron energy loss spectrum (EELS) in Figure 2i at the location of Na filament further indicates a metallic state of the Na filament.[23] A reverse bias was applied after the first Na extraction resulting in Na stripping at the interface. More filaments growing at the same GB were observed during the 2nd Na extraction shown in Figure 2e,f. Comparison of the O, Na, and Al EDX peak area (Figure S2, Supporting Information) measured from a spectrum acquired at a region without filament growth before and after biasing suggests that the Na content of the involved grains (G1 and G2) was maintained from the initial state throughout the prolonged biasing. Moreover, the same crystal structure and orientation was observed by the nanobeam electron diffraction (NBED) before (Figure 2g) and after Na-filament growth (Figure 2h) for grain G1. The conservation of the Na content in the grains and their identical crystal structure before and after filament formation shows that the Na-filament growth was not induced by local electric field-driven degradation of the Na-β''-alumina. This proves that anodic degradation as has been reported for beta alumina at high temperatures[21,22,24–27] is not an issue in these experiments. The observed Na growth in the field of view is due to a process combining Na^+ migration towards the W tip and Na^+ reduction and deposition at the Au(Pt) electrode as well as at the GB.

ADVANCED
SCIENCE NEWS

www.advancedsciencenews.com

ADVANCED
ENERGY
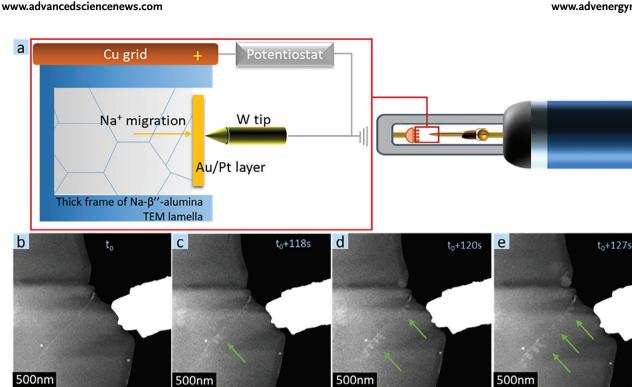**MATERIALS**

www.advenergymat.de

Figure 1. a) In situ biasing TEM setup with a focused ion beam (FIB) processed Na-β''-alumina TEM lamella attached to a Cu grid, which was connected to a grounded W tip. While the thick Na-β''-alumina frame at the positive electrode (Cu grid) was sacrificed as Na source, cathodic sodium deposition occurred at the Au(Pt) electrode by Na$^+$ migration towards the negative electrode (in this case, Au(Pt) layer) driven by the externally applied bias as indicated by yellow arrow. b–e) Time series of high-angle annular dark field scanning transmission electron microscopy (HAADF-STEM) images of the Na-β''-alumina locally in contact with the W tip showing the Na filament growth (indicated by green arrows) at a GB during biasing.

To investigate electron beam effects on the sample and in particular on the Na filament growth, reference experiments were carried out with the electron beam blanked throughout the complete biasing. The features observed in this reference were analogous to the experiments with the beam on: besides Na deposition at the interface between Na-β''-alumina and Au(Pt) electrode, a Na filament was also observed at a GB after biasing as shown in Figure S3b,c (Supporting Information). Therefore, we conclude that both observations are inherently resulting from the applied external electric field, whereas electron beam effects only play a minor role.

The mechanism controlling Na nucleation and filament growth is expected to be similar to Li filament formation in ASSBs, i.e., highly dependent on the local electronic and ionic transport properties of the SE.[28] On the one hand, the local gradient in the (electronic/ionic) transference numbers is one of the key factors resulting in metal nucleation under the influence of sufficiently high current densities.[29] Furthermore, a reduced band gap as small as 1–3 eV was observed for some GBs in oxide SEs[8] and its surface can trap excess electrons within polycrystalline Li SEs.[30] On the other hand, an ionic bottleneck has been speculated to be a reason leading to an overshoot of the local chemical potential of lithium, which builds up a driving force for lithium nucleation.[29,31] In the Na counterparts, Na filament growth at GBs indicated that the blocked Na$^+$ ions do not easily migrate across GBs. However, the origin of the local overpotential and blocking Na$^+$ ions at GBs has not been identified so far.

To identify this origin for Na-β''-alumina and to explore the effect of the microstructure on Na$^+$ ion migration and Na filament growth, in situ biasing TEM measurements were carried out on lamellae with multiple grains present as shown in **Figure 3**a. Since the contrast in HAADF-STEM imaging (Figure 3a) does not allow to uniquely identify all grain boundary features in the polycrystalline material, the microstructure of the thinned region of the lamella (dark green inset rectangle in Figure 3a) was analyzed by 4D-STEM based diffraction mapping (Figure S4A,B, Supporting Information). The virtual dark field images of individual grains (Figures S4g–l and S5j–r, Supporting Information) were generated based on the distinct diffraction reflections (Figures S4a–f and S5a–i, Supporting Information) in the 4D-STEM data cube and GBs were marked in the HAADF-STEM image in Figure 3 for tracking Na filament formation during the in situ measurement. Prior to the analysis, the Na-β''-alumina surface has been uniformly coated with a thin Au(Pt) layer, which acts as an electrode for this setup and ensures uniform potential of all grains next to the Au(Pt) layer when applying a bias voltage at the W tip of the in situ TEM holder. During biasing, we observed that Na segregated outside the grains and formed small filamentary seeds growing with time. The real-time observation of the Na filaments formation is presented in Figure 3b–e.

The first Na filament growth including the sodium-gold alloy reaction appeared at various irregularly spaced positions at the interface between Na-β''-alumina and Au(Pt) electrode (indicated as P1 to P3 in Figure 3c), and afterwards within the Na-β''-alumina (indicated as P4 in Figure 3d). During the early stages of Na
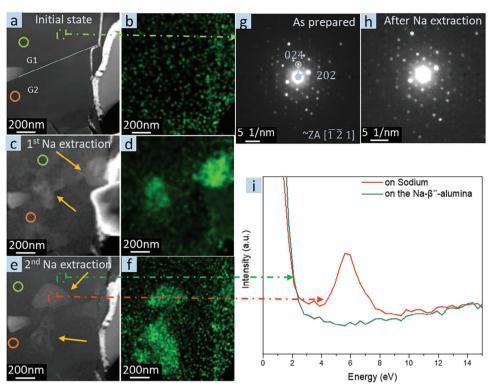
Figure 2. Comparison of the crystal structure and Na content between the initial state and after Na extraction: a–f) HAADF-STEM imaging and EDX Na maps: a,b) initial state, c,d) after 1st Na extraction, e,f) after 2nd Na extraction; Two distinctive grains of Na-β''-alumina denoted as G1 and G2 and the corresponding GB is marked by the light blue line in (a). Na filament positions are highlighted by yellow arrows. A reverse bias was applied between the 1st and 2nd Na extraction and Na was stripped. g,h) Nano-beam electron diffraction (NBED) pattern of G1 in the pristine state and after Na extraction; i) Low loss EELS of an area with Na filament growth (orange) and adjacent free area (green). The EDX spectra averaged for the region marked by the green and orange circle are plotted in Figure S2 (Supporting Information).

filament growth, the HAADF-STEM contrast is not too high making it difficult to clearly see the filaments in the direct image, but the differential images (Figure S6a,b, Supporting Information) also confirmed the morphology changes, which were assigned as Na filament seeds. The growth of Na filament P4 started at the GB between grains G11 and G16 (Figure S6b,c, Supporting Information). The filament itself is unconnected to the Au(Pt) electrode, but the corresponding GB ends at the Au(Pt) electrode. Further biasing resulted in growth of the existing filaments and more filament seeds appeared along the GB between G11 and G16 (Figure S7, Supporting Information) until it was mostly covered as shown in Figure 3e,f. This suggests that Na+ ions were blocked by the GB from G11 to G16. Finally, Na filaments (indicated as P5 and P6 in Figure 3f) also appeared at the GB between G11 and G15. Apparently, they only started to grow after establishing sufficient electric contact with the Au(Pt) layer through the Na filament at the GB between G11 and G16. Interestingly, when the filament formation reached the triple boundary of G11, G15, and G16, filament growth was mainly observed at the GB G11/G15 and only to a limited amount at the GB G15/G16 (small filaments label as P7 in Figure 3f) based on the size of the filaments. This shows that more Na+ ions are blocked and reduced at GB G11/G15 than at GB G15/G16 indicating that various GBs exhibit different behavior for the Na filament growth.

Looking at the Na filaments, they mostly exhibit a roundish shape and do not show well-developed faceting or geometries.

This has previously been attributed to small currents and small volumes of Na filaments.[32] In addition to the Na filament growth on the thin region of the TEM lamella, larger well-faceted whiskers were observed growing from the backbone of the lamella (Figure S8, Supporting Information). This indicates that the Na filament does not only appear in the thin region but also in the thick region that was far from the Au(Pt) electrode. However, we did not further investigate the origin for the sodium reduction in this area.

The Na filaments observed during the in situ biasing experiments are mainly located on the surface of the SE, which can be attributed to the lack of mechanical back stress for filament formation out of the TEM lamella into the vacuum. Nevertheless, the filament formation is presumably initiated inside the sample starting from sodium gold alloy formation in case of the filaments formed close to the electrode. After the in situ biasing experiment, the Na filaments growing out of the TEM sample surface were removed by FIB cleaning. STEM analysis of the cleaned lamella reveals the existence of a pronounced crack along the entire G11/G16 GB as shown in Figure 3g. This shows that underneath the observed Na filament on the surface, sodium is also growing within the GB. This was presumably the starting point for the filament formation.[9,33] This crack formation at the GB will decrease the overall ionic conductivity and mechanical strength.

**ADVANCED
SCIENCE NEWS**

www.advancedsciencenews.com

**ADVANCED
ENERGY
MATERIALS**
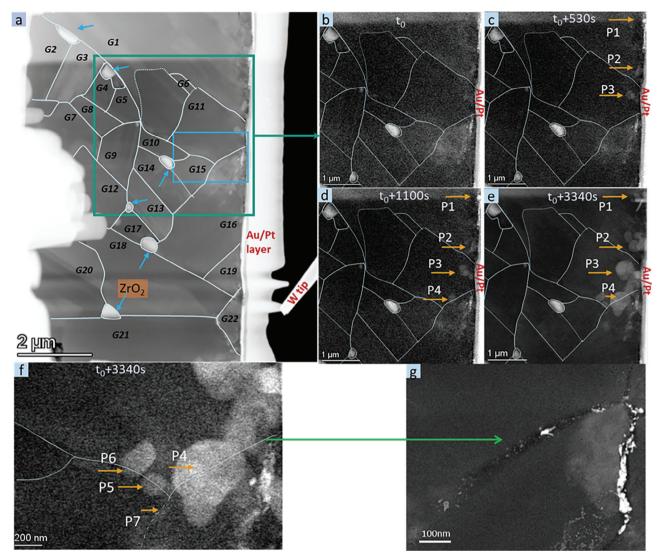
www.advenergymat.de

Figure 3. Time series HAADF-STEM images during biasing showing Na filament growth: a) HAADF-STEM image of the whole thinned area of the TEM lamella with GBs indicated by white lines and the different grains labeled. The bright particles are ZrO_2 particles (blue arrows) used as additive during synthesis. b–e) The morphological evolution of the area marked by the dark green rectangle in (a) with time during biasing; The Na filament positions are indicated by yellow arrows and labeled. f) Magnified image of the area marked by the blue rectangle in (a) after 3340s of biasing. g) HAADF-STEM image of the region around P4, which was polished by FIB after in situ TEM measurements. A crack at the GB underneath P4 became visible.

2.2. Understanding the Influence of the Microstructure on the Na Filament Growth

To assess the factors leading to the local differences in Na$^+$ ion transport and the formation of filaments, crystallographic information including crystal orientation and GB classification was obtained from automated crystal orientation map (ACOM) analysis based on precession electron diffraction on many positions in each individual grain as schematically illustrated in **Figure 4**a. Based on the subsequently calculated Euler angles representing the grain orientation, the crystallographic relationship of adjacent grains was computed. With this, a simplified model for the orientation of the Na- β''-alumina atomic structure for each individual grain was generated, which is schematically illustration in Figure 4b.

Looking at the Na filaments (P1 to P4) that formed at the Na-β''-alumina│Au(Pt) interface, here the higher Na$^+$ ion-conducting directions (orientations) are aligned towards the Au(Pt) electrode as indicated for grains G1, G11, and G16 (Figure 4b). As a consequence, Na$^+$ ion migration towards the electrode and accumulation at the interface was facilitated under the applied electric field. Once Na$^+$ ions reached the electrode, they were reduced to Na^0 following the nucleation and growth as the electronic and ionic pathways meet. Therefore, it was common to find the initial sodium growth as plating close to the interface with the electrode. The inhomogeneous growth of Na filaments can presumably be attributed to defects in the grains, either intrinsic or introduced during sample preparation. More electrons are trapped at defects, which then contribute to the Na$^+$ ion reduction and growth of Na filaments. In addition, we like to point out that we did not observe
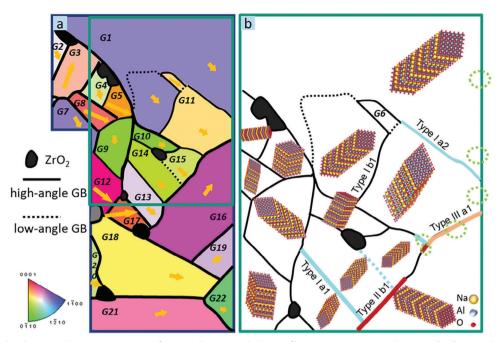
Figure 4. Relationship between the microstructure of Na-β''-alumina and the Na filament position. a) Schematically illustrated orientation map of the whole lamella (Figure 3a) where the yellow arrows represent the direction of fast Na$^+$ ion migration in the individual grains with their length indicating the angle between the Na$^+$ ion conduction plane and the surface of the lamella. The longer the arrow the more parallel is the conduction plane of Na-β''-alumina to the surface of the lamella. The orientation of grains was obtained by automatic crystal orientation map analysis (Figure S9, Supporting Information). The color indications for different crystallographic orientations as indicated in the inverse pole figure. b) Crystal structure models representing the orientation in the individual grains in the area indicated by the dark green rectangle in a. Solid lines represent high-angle GBs (HAGBs), while dashed lines indicate low-angle GBs (LAGBs). The color coding of the GBs in b follows **Figure 5**. The green dashed circles indicate the region where Na filaments grew during biasing.

Na plating at the interface between the Au(Pt) electrode and other grains such as G19 and G22. As we will show later on, there was insufficient Na$^+$ ion transport at the lower part of the lamella due to the electrode arrangement.

In addition to the overall effect of the distinctive orientation-dependent ion transport properties of the grains in Na-β''-alumina[34] and considering the importance of grain orientation in Na plating at the interface with the Au(Pt) electrode, we hypothesize that Na segregation and filament growth at GBs will be influenced by the crystallographic relationship between neighboring grains and their overall orientation. The indexed ACOM data indicates an overall random grain orientation, as depicted in Figure 4b. For key grains involved in the Na filament formation, the corresponding GB misorientation angles are summarized in Table S1 (Supporting Information). GB misorientation angles above 15° indicate that the material is dominated by high-angle GBs (HAGBs) analogous to oxide-type Li solid electrolytes,[14] except for low-angle GBs (LAGBs) between G14 and G15 as well as G6 and G11. Among all of the HAGBs, only two coincidence site lattices (CSL) boundaries have been observed, a $\sum 3$ between G13 and G14 and a $\sum 21$ boundary between G5 and G6. The interface associated with both GBs includes a (0 0 1) facet, where it is widely accepted that the Al-O spinel blocks on the (0 0 1) facets impede Na$^+$ ion out-of-plane migration significantly. A similar blocking effect is expected for these GBs, indicating that the resistivity for Na$^+$ ion migration varies depending on the crystallographic relationships between adjacent grains. Interestingly, overall, GBs with coincidence lattice relations, which are most

commonly considered in simulation models for ionic conductivity and activation energy calculations, constitute a minority of the GBs in the SE, which is dominated by random HAGBs.

Based on the misorientation of adjacent grains determined from the ACOM analysis, it is also possible to calculate the angle between the fast Na$^+$ ion transport planes in both grains (Table S1, Supporting Information). The crystallographic misorientation angle and the angle between the Na$^+$ ion conduction planes for the two orientations are not necessarily the same. As the angle between the Na$^+$ ion conduction planes determines the Na$^+$ ion transport properties across the GB, we use this information to estimate the anisotropic transport behavior across GBs. To analyze the impact of the microstructure on the Na$^+$ ion transport and the Na filament growth, we coupled the misorientation of Na$^+$ ion conduction planes between adjacent grains and the local applied electric field direction. As a simplified description, we classified the orientation relation between the Na$^+$ ion conduction planes into 3 main types: parallel (Type I), perpendicular (Type II), and oblique (Type III), which we further subdivided based on the angle between GB and the conductive plane direction. Finally, we distinguished their orientation with respect to the external electric field direction as is schematically shown in Figure 5.

For the GBs depicted in Figure 5 as type I, adjacent grains can have arbitrary misorientation angles. However, their Na$^+$ ion conduction planes are parallel and aligned for ion migration in an electric field. These planes can either be parallel to the GB and disconnected, separated by an Al–O spinel layer (Type I a) or be aligned and connected across the GB (Type I b). In both cases, the
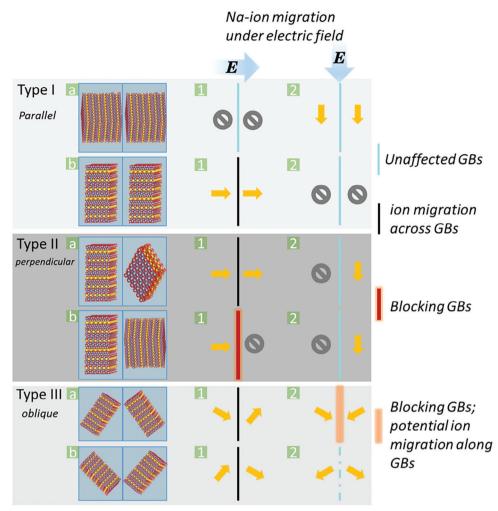
Figure 5. Schematic illustration of the relationship between the orientations of adjacent grains and the direction of the Na$^+$ ion transport in the external electric field. The orientation relationship of Na$^+$ ion conduction planes in adjacent grains was classified into three main types: parallel (Type I), perpendicular (Type II), and oblique (Type III). The Na$^+$ ion transport paths for different directions of the external electric field (blue arrows) are indicated by orange arrows and gray circles. Depending on the orientation of Na$^+$ ion conduction planes, GBs exhibited different migration behavior: without migration across the GB (cyan), migration across the GB (black), and blockade of the ion migration (red and orange). The difference between the orange and red boundary is due to the possibility for ion transport along the GB in case of the orange boundary.

ion transport paths between neighboring grains share the same direction. This implies that the blocking behavior of these GBs is limited. Depending on the electric field direction, they are either not involved in the ion migration or only result in a limited obstacle at structural distortions at the GB. In the depicted specimen, for instance, the relationship between grains G13 and G14 as well as G14 and G15 is considered to be of Type I a, while the relationship between grains G6 and G11 is close to the Type I b, as shown in Figure 4.

In addition to the case of parallel Na$^+$ ion conduction planes, a relatively weak blocking effect of GBs would also be expected for adjacent grains with perpendicular Na$^+$ ion conduction planes oriented as illustrated in Type II a. In contrast, GBs of Type II b would block Na$^+$ ion migration across the GB due to the dense Al-O spinel layer aligned along the GB. This blockade of the ion migration across the GB will occur independent of the orientation of the left grain, leading to an accumulation of Na$^+$ ions at this type of GB and eventually will limit further transport to the

GB. An example for this configuration can be seen in Figure 4, where the GB between grains G14 and G16 as well as G15 and G16 corresponds to Type II b1. However, with the same basic GB orientation, but the electric field oriented parallel to the GB as in type II a2 and II b2, the GBs would not affect transport properties. This demonstrates the critical interplay between the electric field direction and the orientation of Na$^+$ ion planes.

The more general case of GBs with an oblique orientation relationship of the Na$^+$ ion plane direction in neighboring grains is depicted as type III. This orientation relationship is the most common one observed in randomly oriented polycrystalline Na-β''-alumina, as can be experimentally seen, e.g., for GBs G10/G15, G9/G14, and G12/G13. In this case, the Na$^+$ ion transport behavior critically depends on the relative orientation to the external electric field. With the electric field aligned across the boundary as in type III a1 & b1, some ion transport across the GB is expected to be possible. The misorientation of the Na$^+$ ion planes affects the driving force of Na$^+$ ion migration in adjacent

ADVANCED
SCIENCE NEWS

www.advancedsciencenews.com

ADVANCED
ENERGY
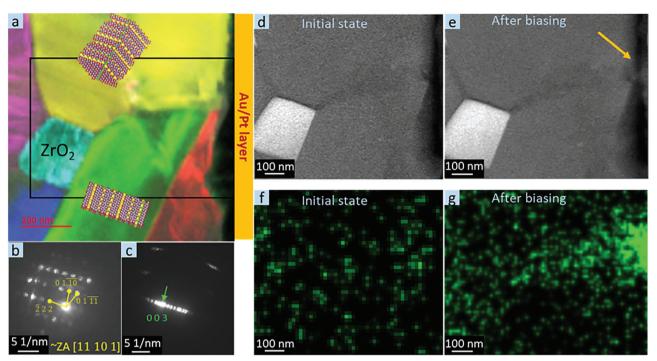**MATERIALS**

www.advenergymat.de

Figure 6. Na filament growth at the triple junction between a type III b2 GB and the Au(Pt) layer. a) RGB-coded grain map based on 4D-STEM. The position of Au(Pt) layer is schematically indicated. The crystal orientation for the yellow and green grains was obtained based on b,c) their corresponding NBEDs. d) HAADF-STEM image of the pristine state of the area indicated by the black rectangle in (a). e) HAADF-STEM image of the same region after biasing for 1400s. The Na filament is indicated by an orange arrow. Low-dose EDX Na map of the specimen at f) initial state and g) after biasing.

grains, which depends on the component of the electric field in the direction of each grain's Na$^+$ ion plane. Consequently, the direction of the external electric field and the misorientation angle between the Na$^+$ ion planes influence the Na$^+$ ion flux and potential blockage between adjacent grains. Experimentally, we often observe a relatively large misorientation of the transport direction between adjacent grains. For instance, the GBs G5/G9, G8/G9, and G9/G13 with a misorientation of the Na$^+$ ion transport path direction of 66°, 66°, and 53° belong to this type when an external electric field is applied. In case of type III GB, the GB is expected to noticeably affect the ion transport properties even in case the applied electric field is parallel to the GB as depicted for type III a2 & b2. For type III a2, the electric field parallel to the GB will drive Na$^+$ ion towards the GB from both sides. Depending on the ion mobility along the GB, this will result in a blockade of Na$^+$ or enhanced transport along the boundary. Experimentally, this type of boundary is observed at the GB G11/G16, in which Na filament initial growth was observed as shown in Figure 3d. Moreover, the GB where we observed the growth of Na in the beam-blank experiment as seen in Figure S3b (Supporting Information) also belongs to this type (Figure S3e, Supporting Information). This can be attributed to electron injection from the Au(Pt) electrode and the high number of Na$^+$ ions at the GB, which facilitates the nucleation and growth of Na filaments. However, in other experiments with similar GB geometries belonging to type III b2, we observed Na segregation at the triple junction between the GB and the Au(Pt) electrode as shown in **Figure 6**. The high Na signal at the triple junction after biasing strongly suggests fast Na$^+$ ion transport along the GB leading to the segregation at the triple boundary among the grains and Au(Pt) electrode in this case.

Except for GB G11/G16, all other GBs directly connected to the Au(Pt) electrode did not exhibit any Na filament growth, e.g., GB G1/G11 as shown in Figure 3e. This can be attributed to its GB type I a2. As depicted in Figure 4b grains G1 and G11 possess parallel similar Na$^+$ ion transport paths. Therefore, in contrast to GB G11/G16, GB G1/G11 does not lead to Na$^+$ ion blockage, which seems to favor Na filament formation at GB G11/G16.

In addition to the grain orientation and GBs, the ZrO$_2$ impurities are a non-negligible microstructural feature in this Na-β''-alumina SE, which locally disturb Na$^+$ ion transport. However, during the limited time of the in situ experiments, we did not observe a specific contribution to the Na filament growth.

2.3. Simulation of the Microstructure Affected Na$^+$ Ion Transport in Na-β''-Alumina

The setup used for the in situ experiments is slightly unusual as the electrodes are not opposite to each other, but at a 90° angle (see **Figure 7**a). The corresponding electric field distribution not considering any microstructure of the Na-β''-alumina in between is shown in Figure 7e. Even without considering the microstructure, this results in a current that is not distributed uniformly, but exhibits a gradient as shown in Figure 7b with more than an order of magnitude difference between the upper part of the structure and the bottom. Based on this configuration, the current distribution in the system was modeled when the experimentally determined microstructure is considered (Figure 7c,d), i.e., the anisotropic transport within each grain and assuming a certain GB ionic conductivity, while not considering diffusion
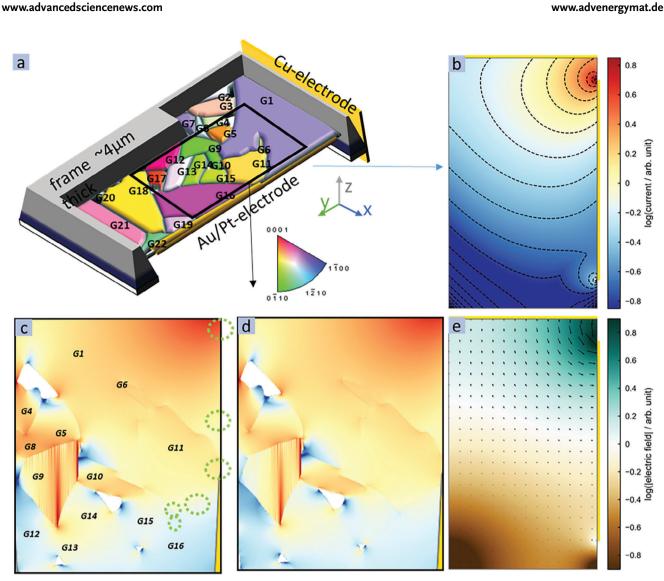
**ADVANCED
SCIENCE NEWS**

www.advancedsciencenews.com

**ADVANCED
ENERGY
MATERIALS**

www.advenergymat.de

Figure 7. Computational modeling of the current density distribution for the in situ TEM setup: a) Schematic representation of setup. b) Current density distribution only considering the external circuit with a uniform isotropic SE between the electrodes (yellow rectangles at top and right). The isocurrent lines are marked. c) Current density distribution based on the microstructure of the thin region of TEM lamella. The thick frame around the TEM lamella was not considered. d) Current density distribution based on the microstructure of the thin region of the TEM lamella and approximating the thick frame around the thin TEM lamella as an isotropic medium with an effective ionic conductivity two orders of magnitude lower than in-plane ionic conductivity in Na-β''-alumina. The green dashed circles indicate the positions of the Na-filaments in the experiment. e) Electric field distribution only considering the external circuit with a uniform isotropic SE between the electrodes (yellow rectangles at top and right). The arrows indicate the direction. The electric field distribution based on the microstructure is depicted in Figures S10c and S11c (Supporting Information).

along GBs. Details of the simulations are included in the method section and supplementary information. As the microstructure in the thick frame around the lamella is unknown, we considered two computational models: the reduced system (Figure 7c), which neglects any contribution of the thick frame to the Na$^+$ ion transport, and the full system (Figure 7d), which assumes an isotropic effective conductivity for the thick frame.

Both, the reduced and the full system exhibit a distinct distribution of the calculated current density for different grains even between neighboring grains. For example, compared to corresponding areas without microstructure (Figure 7b), the anisotropic microstructure results in a highly enhanced current density for G10. It is even higher than the one in G1

and G11, which are closer to the electrodes (Figure 7c,d). This clearly demonstrates the importance of the microstructure and the anisotropic Na$^+$ ion transport in Na-β''-alumina on the local current density in the material. These results are in qualitative agreement with the simplified picture for the ion transport in adjacent grains developed in Figure 5.

Moreover, the simulations indicate apparent current density differences, e.g., between grains G11/G16, G10/G15, G9/G13, and G9/G14 due to the large misorientation of their Na$^+$ ion transport paths as shown in Figure 7c,d. This suggests blockage of the Na$^+$ ion migration across these GBs and results in a high local electric field at GBs (see Figure S10c, Supporting Information). Hence, an elevated chemical potential of Na metal

**ADVANCED
SCIENCE NEWS**

www.advancedsciencenews.com

**ADVANCED
ENERGY
MATERIALS**

www.advenergymat.de

(i.e., $\mu_{Na} > \mu_{Na}^0$) can develop between these adjacent grains during biasing, in line with the mode 2 mechanism detailed by Krauskopf et al.[29,31,35]. Nevertheless, the Na filament growth was only observed at GB G11/G16, but not at the other three GBs with large current differences. This is presumably attributed to their different electronic properties, their distances to the electrode, and the activation barrier that has to be overcome for nucleation.[29,36,37] As GB G11/G16 is directly connected to the Au(Pt) electrode, an effective overpotential was gained for the first Na nucleation at this GB.[28,38] For GBs G10/G15, G9/G13, and G9/G14, far from the interface with the Au(Pt) electrode, the local increase of the chemical potential developed in the experiment is apparently not sufficient for driving Na reduction and nucleation. However, it has been speculated that Na filament growth inside bulk Na-β''-alumina may occur once the local excess chemical potential reaches the nucleation driving force at the GBs as the Na whiskers were observed growing from the thick frame as shown in Figure S8 (Supporting Information). Notably, other GBs directly connected to the Au(Pt) interface such as G1/G11, G16/G19, and G19/G22 did not exhibit Na filament growth. In the case of G16/G19 and G19/G22 this might be due to the fact that there is only minor ion transport in those grains. However, in case of grains G1 and G11 the current is high, but the current density difference is not remarkable as shown in Figure 7c,d and Figures S8,S9 (Supporting Information), suggesting no significant blocking behavior of G1/G11 in agreement with the simplified model of type I a2 in Figure 5.

In addition, during the later stages of in situ biasing, significant Na filament formation at GB G11/G15 was observed, while only limited filament formation occurred at GB G15/G16. This is in line with the simulated current density at those two GBs. Moreover, since only the ionic conductivity across GBs was considered in this model, whereas ion transport along GBs was not included, we would also speculate that the current density difference between G11/G15 may be even higher due to contributions from G10, which shows a high current density, via the triple boundary with G11/G15. Consequently, the filament size at GB G11/G15 was much larger than at GB G15/G16.

2.4. Post-Mortem Characterization of Cycled Na-β''-Alumina

To investigate the cycled behavior of bulk Na-β''-alumina, the symmetrical Na│Na-β''-alumina│Na cell was assembled to characterize the electrochemical cyclic aging process. The cross-section of the cycled Na-β''-alumina was produced for ToF-SIMS analysis. We found an evident Na segregation of cycled Na-β''-alumina through ToF-SIMS 2D and 3D Na maps as shown in **Figure 8**a,d. Since Na mapping for the as-prepared Na-β''-alumina (as shown in Figure S12d,h, Supporting Information) show a nearly uniform distribution with the same consumption of ion dose during the SIMS analysis process as for the cycled specimen, it can be assumed that the obvious segregation was induced by the cyclic process. Due to the limited resolution of the Na maps, the nanometer thin Na filaments were not considered. It was found that Na segregation was distributed mainly in three types of morphological features in 2D Na maps: the isolated non-regular micron-sized Na particles (as gold arrows pointed in Figure 8 and Figure S12, Supporting Information), the connec-

tion of the micron-sized Na particles and zig-zag line-shaped Na filaments (as green arrows pointed in Figure 8 and Figure S13, Supporting Information), and the line-shaped Na filaments (as blue arrows pointed in Figure 8a,d and Figure S13b, Supporting Information). The micron-sized Na particles were found filling in the voids of Na-β''-alumina as shown in the correlative SEM image (Figure 8b) to the inset rectangle region in Na map (Figure 8a). The side view of 3D Na and overlaid maps indicated that these voids were fully occupied as shown in Figure 8d,e. Tian et al. revealed that significant excess electrons can be trapped on the surface of some oxide electrolytes, e.g., LLZO due to their lower band gap compared to the bulk.[29] Moreover, lower mechanical energy dependent on the induced back stress of surrounding grains can contribute to the Li dendrite growth.[36] The analog Na growth in voids within Na-β''-alumina can be attributed to the low band gap of the surface and absence of the back stress. In addition to the micron-sized Na particles, the line-shaped Na filaments were figured out always along the GBs in the correlative SEM image in Figure 8b. Most of the GBs, which were connected to micron-sized Na in voids, were filled with small amount of Na filaments as shown in Figure 8a,b. We suggest that the Na probably grew in the voids first, which behaved like a reservoir to store the Na, and enable further nucleation at the adjacent GBs for facilitating the penetration of Na along the GBs. Furthermore, the isolated line-shape Na appearing in the Na map (see Figure 8a,d and Figure S13b, Supporting Information) indicated that Na-filament growth initiated from GBs inside the bulk electrolyte during cycling. This observation was in line with the above prediction. In addition, the thick line-shaped Na filaments were recognized as cracks through the Na and Al maps in Figure S12 (Supporting Information). This is caused by the strain induced by the large Na-filament growth.

Furthermore, similar to the in situ TEM observations, we did not find any correlation between the side phase of ZrO_2 and the location of Na filaments in the cycled specimen as shown in Figure S12a,e (Supporting Information). It suggested that ZrO_2 may not contribute to the sodium nucleation and worsen the Na filament growth.

2.5. Na Filament Network along Inner Na-β''-Alumina Boundaries

Based on the experimental in situ biasing results in combination with simulation and the post-mortem analysis, Na filament growth appears to be a critical phenomenon in the Na-β''-alumina electrolyte, which strongly depends on the local microstructure. It can initiate from the interface between Na metal and SE, where GBs are located as illustrated in **Figure 9**a. These GBs can either exhibit a high resistance for transport or allow fast ion transport depending on GB structure and orientation. Moreover, the anisotropic ion transport results in GBs inside the SE that are strongly blocking Na$^+$ ion transport, which can also be an origin for Na nucleation with a sufficient overshoot of the Na chemical potential (μ_{Na}). Since this blocking behavior can occur for a wide range of GB orientations relative to the external electric field as depicted in Figure 5, Na nucleation can take place at these GBs. Apart from GBs, our SIMS analysis further suggests that voids act as sinks for Na and the filling is usually
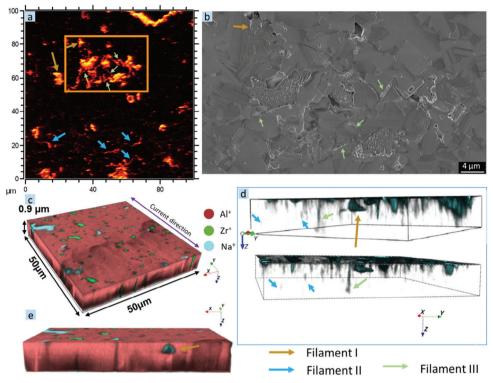
**ADVANCED
SCIENCE NEWS**

www.advancedsciencenews.com

**ADVANCED
ENERGY
MATERIALS**

www.advenergymat.de

Figure 8. Time-of-flight secondary ion mass spectrometry (ToF-SIMS) maps and correlated scanning electron microscopy (SEM) image of Na-β''-alumina after cycling in a Na │ Na-β''-alumina │ Na cell for 110 cycles; a) ToF-SIMS 2D map of Na$^+$ (Field of view: 100 µm × 100 µm); Al$^+$, Zr$^+$, and their overlaid maps are shown in Figure S12a–c (Supporting Information). b) Correlative SEM image of the area marked by the rectangle in (a); The mapping and imaging directions are aligned with the applied current direction; c) ToF-SIMS 3D surface rendering of the sputtered volume of 0.9 µm × 50 µm × 50 µm with an overlay of Al$^+$, Zr$^+$, and Na$^+$; d. side view of the Na$^+$ distribution in 3D (c); e) 3D surface rendering oriented with the short axis along the z direction of sputter removal. ToF-SIMS 3D surface rendering of another area was depicted in Figure S13 (Supporting Information). Three types of Na filament: Filament I (isolated micron-sized Na particles) was pointed by the gold arrows; Filament II (isolated line-shaped Na filaments) were pointed by the blue arrows; Filament III (the connection of micron Na particles and line-shaped Na filaments) were pointed by the green arrows.

accompanied by filament penetration along GBs. Therefore, a Na-filament network (Figure 9b) can be formed in the Na-β''-alumina during Na cyclic deposition process subsequently leading to a failure of the battery.

3. Conclusions

In this work, we conducted in situ biasing experiments to investigate Na transport and deposition in a Na-β''-alumina │ Au(Pt) multilayer system in a TEM at room temperature. Na deposition occurred not only at the interface between Na-β''-alumina

and Au(Pt) but also at selected GBs in the Na-β''-alumina "bulk." Na filament growth mainly started along GBs connected to the Au(Pt) electrode. From this GB Na filament formation penetrated to neighboring GBs. In addition, Na whiskers grew from the thick frame of TEM lamella. This indicates that Na filament growth can initiate both from GBs at the interface between the SE and the negative electrode as well as inside the SE. Moreover, we could show that Na$^+$ ion diffusion is enhanced along some GBs, as Na metal accumulated at triple boundaries between the GB and the Au(Pt) electrode. In addition to GBs, voids can also act Na sink during the Na plating process based on the post-mortem SIMS
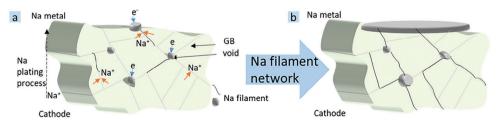

Figure 9. Na filament network formation in the Na-β''-alumina based on its microstructure. a) During Na plating, Na filaments can form starting at the interface between Na-β''-alumina and Na metal anode as well as within Na-β''-alumina, i.e., at some blocking GBs with oblique orientation and at voids where sodium can nucleate. b) Subsequent Na plating processes facilitate the penetration of Na filaments along GBs, leading to the formation of a network that connects the Na metal anode and cathode.

analysis of cycled Na-β''-alumina, probably due to potential differences at the void surface/GBs. Nevertheless, neither in situ biasing experiments nor post-mortem analysis demonstrated any relationship between the ZrO_2 additive and Na filament growth. Overall, depending on the local microstructure, the anisotropic transport in Na-β''-alumina leads to Na filament network formation along GBs and voids during cyclic Na deposition, which subsequently induce the failure of the cell.

The relationship between the microstructure and Na filament growth as well as Na$^+$ ion transport was explored by crystal orientation analysis, which revealed randomly oriented crystals in the polycrystalline Na-β''-alumina mostly connected by random HAGBs, whereas hardly any CSL boundaries have been observed. Na filament growth occurred at random HAGBs. Since Na-β''-alumina has a typical layered structure resulting in a 2D ion transport path, the influence of the anisotropic ion transport on the effect of GBs to the Na$^+$ ion transport was investigated based on the combination of the orientation of the Na$^+$ ion planes and the electric field direction.

In a simplified microstructural model, three groups of GBs were defined based on the orientation relationship of the Na$^+$ ion planes in adjacent grains: parallel (type I), vertical (type II), and oblique (type III). The blocking behavior for ion migration at GBs depends on the relative orientation of the Na$^+$ ion conducting planes in adjacent grains and the direction of the external electric field. In the proposed model, two cases result in blockade of ion migration across GBs: 1. In type II b1, the dense Al-O spinel layer in one grain blocks ion transport at the GB from the neighboring grain where the Na$^+$ ion conduction planes are parallel to the external electric field and oriented towards the GB. 2. In Type III a2, Na$^+$ ions in two adjacent grains migrate towards their common GB and, if the ion conductivity along the GB is limited, this leads to blockade of Na$^+$ ion transport. This blockade at GBs seems to facilitate formation of Na filaments and should be avoided to improve the stability of the solid electrolyte. Moreover, simulations of the microscopic Na$^+$ ion transport in the TEM-lamella demonstrated a significant influence of the anisotropic Na$^+$ ion migration, resulting in a highly inhomogeneous current density distribution in the specimen. Therefore, the microstructure including GB types and orientation should be taken into account for optimizing oxide based SE performance both in terms of Na filament formation as well as overall ionic conductivity. Highly textured SEs with their Na$^+$ ion conducting planes oriented along the external electric field would significantly improve the overall ion conductivity and reduce the presence of GBs blocking Na$^+$ ion transport and thus would be expected to prevent Na filament formation.

4. Experimental Section

In Situ TEM Characterization: Polycrystalline Na-β''-alumina SE pellets (Ionotec. Ltd, UK, phase content 90–95%) were used in this work. To get access to their GBs in the TEM, a focused ion beam (FIB) (FEI Strata 400S) was applied to obtain TEM lamellas with around 4 μm x 5 μm large and ≈170 nm thick electron transparent area. A ≈100 nm thick Au layer was coated before any TEM experiment to the surface of Na-β''-alumina pellet to minimize the charge effect and electric field induced damage during FIB process. Moreover, this Au layer served as the negative electrode together with the Pt layer, which is deposited for FIB process, during the

in situ electric biasing TEM measurements. The double aberration corrected Themis Z (ThermoFisher Scientific) and probe corrected Themis 300 TEMs (ThermoFisher Scientific) operated at 300 kV were used for TEM analysis. With the usage of scanning tunneling microscopy-transmission electron microscopy (STM-TEM) holder (ZEPtools Technology Company, PicoFemto double-tilt holder), the in situ TEM setup (schematic illustration in Figure 1a) was built to provide the electrical biasing to the lamellae and worked as shown in time series images as Figures 1b–e and 3b–e. Once the W tip was contacted to the specimen, a positive voltage in the range of 10 – 17 V was applied to the TEM Cu grid. Therefore, the Na$^+$ ions were driven toward the W tip as well as the Au(Pt) deposition layer side. Meanwhile, high-angle annular dark field scanning transmission electron microscopy (HAADF-STEM) series images were acquired to record the morphological changes. The low-dose energy dispersive X-ray spectroscopy (EDX) (Super-X EDS detector) elemental mapping was used to explore the composition distribution. Advanced TEM techniques of 4D-STEM and automated crystal orientation map (ACOM) analysis (Nanomegas, OIM) were employed to investigate the microstructure of Na-β''-alumina. The electron beam diameter was nominally 170 pm with a convergence angle of 30 mrad and a screen current of 50 pA to conduct the ADF-STEM imaging, while the microprobe with a convergence angle of 0.5 mrad was carried out for 4D-STEM and ACOM. To eliminate the influence of the electron beam on the material, a beam-blank experiment was conducted as a reference to in situ beam-on TEM experiment. This procedure is explained in detail in the supplementary information.

Modeling the Current Density Distribution of Polycrystalline Na-β''-Alumina: For the Na$^+$ ion transport modeling in the polycrystalline Na-β''-alumina, the actual microstructure of the whole TEM lamella was generated based on the HAADF-STEM image (Figure 3a), the 4D-STEM grain map (Figure S3A, Supporting Information), and the ACOM map (Figure S5, Supporting Information). The 2D surface information is discretized into an array of a single layer of cubic voxels. Each voxel is assigned to a specific grain G_i in the microstructure, to ZrO_2 additives in the lamella, or to the electrode. This allows to distinguish different structural situations for the transport modeling, e.g., transport through the bulk of grains, transport across a grain boundary, the insulating behavior of the ZrO_2 additives or the consideration of the charge transfer reaction at the electrode interface.

The 2D transport computations are based on an electric network model recently developed by Eckhardt et al.[39–41] to study the effect of SE microstructure and parent metal|SE interface morphology on the impedance response of the system. The transport description has been simplified by using a resistor network instead of an impedance network to simulate the direct current (DC) distribution in the system. Transport between different voxels is described by local resistors in the electric network, namely $2 \cdot R_{Bulk}$ for bulk transport, $2 \cdot R_{Bulk} + R_{GB}$ for transport across GBs, and $R_{Bulk} + R_{CT} + R_{Elec}$ for the charge transfer reaction at the electrode interface. Note that ZrO_2 additives are considered to be ideally blocking, i.e., $R_{ZrO2} = \infty \, \Omega$. The magnitude of the local resistances R_i depends on the conductivities σ_i and the structural resolution, i.e., $R_i = 1/\sigma_i \cdot L_i/A$ where L_i and A are the length of the transport process and the interface area between two voxels, respectively.

For the 2D transport computations, we assumed a ratio of the in-plane (ip) ionic conductivity (σ_{ip}) to the out-of-plane (op) ionic conductivity (σ_{op}) of $\sigma_{ip} / \sigma_{op} = 10^3$. This is due to the high out-of-plane Na$^+$ ion diffusion activation energy compared to the diffusion along the Na$^+$ ion conducting plane.[42] In addition, the anisotropic character of Na-β''-alumina was taken into account in the simulations. This means that the individual grain conductivities σ_i in x- and y-direction of the 2D sample are not necessarily the same and both rely on the orientation analysis of the TEM lamella. To this end, the projection of Na$^+$ ion planes onto the sample surface was determined for all individual grains as depicted in the ACOM map (see Figure 4). This results in different angles θ of the Na$^+$ ion plane to the x-axis of sample surface (see Figure S14, Supporting Information). As a result, σ_i with $i = (x, y)$ can be expressed as a function of σ_{ip}, σ_{op}, and θ. The detailed equations are included in the Supporting Information.

The thickness of the GB, including the grain core and adjacent space charge region, was estimated to be 1 nm, and an isotropic GB

conductivity was assumed to be 20 times smaller than the in-plane conductivity, i.e., $\sigma_{ip}/\sigma_{GB} = 20$. For the sake of simplicity, ion migration along GBs was only implicitly considered in the simulations. The ionic conductivity of the backbone of the TEM lamella, averaged over several grains with random/unknown orientation, was assumed to be 250 times smaller than the in-plane Na^+ ion conductivity, i.e., $\sigma_{ip} / \sigma_{backbone} = 250$. In addition, the charge transfer reaction at the electrode interface and the transport within the electrode are assumed to be resistance-free. Further details and illustrations can be found in the supplementary information.

Post-Mortem Time-of-Flight Secondary Ion Mass Spectrometry (ToF-SIMS) Characterization on the Cycled Na-β″-Alumina: The symmetrical Na|Na-β″-alumina|Na cell was assembled by isostatically pressing sodium foils on both sides of the Na-β″-alumina separator (Ionotec Ltd. UK, phase content 90–95%) at 100 MPa for 15 min. Galvanostatic cycling of the symmetric cell was performed on a CompreDrive device (rdh, Darmstadt, Germany) in combination with an SP 200 potentiostat (BioLogic Science Instruments). In total, the symmetric cell was cycled 110 times, Figure S15a (Supporting Information). The working electrode (WE) was polarized for 2 min followed by a resting phase of 1 minute until the current direction was reversed followed by the same procedure. Due to the slightly different electrodes areas a current density of 260 µA•cm^{-2} was applied to the WE while 240 µA•cm^{-2} was applied on the counter electrode.

After cycling, the sodium electrodes were removed from the Na-β″-alumina separator using scalpel and the separator was broken to obtain a cross section of the cell. Before SIMS analysis, the cross-section was polished on the WE side with Ar$^+$ ions at 8 kV for 2 h under cryogenic conditions (150 K) using a Leica EM TIC 3X device (Leica Microsystems GmbH, Wetzlar, Germany). For the Na-β″-alumina reference specimen, a cross-section of an untreated Na-β″-alumina sample was polished using the same Ar$^+$ beam conditions as for the cycled Na-β″-alumina separator. A schema of the geometric set up for SIMS analysis is shown in Figure S15b (Supporting Information).

ToF-SIMS analyses were performed on an M6 hybrid SIMS (IONTOF GmbH, Münster, Germany). All ToF-SIMS measurements were carried out in positive-ion mode. The topography mode of the analyzer was activated to increase the total ion count and the liquid ion metal gun (LMIG) was operated in the delayed extraction mode. Imaging was conducted with 60 keV Bi_3^{2+} primary ions at a cycle time of 60 µs as well as low-energy electron flood gun for charge compensation. Both samples were analyzed on an area of 100 µm × 100 µm with 512 × 512 pixel and a total primary ion dose of 2.8×10^{12} cm^{-2}. A mass resolution $m/\Delta m > 1500$ @ m/z 23 (Na$^+$) is obtained. For depth profiling an area of 50 µm × 50 µm with 256 × 256 pixel was analyzed using same LMIG and analyzer setting as for imaging (total ion dose of primary ions = 2.34×10^{14} cm^{-2}). Sputtering was performed with a 2 kV O$_2$ species on an area of 300 µm ×300 µm with a total ion dose of 4.4×10^{18} cm^{-2}. A mass resolution of $m/\Delta m > 500$ @ m/z 23 (Na$^+$) is achieved. Depth of the sputter creators was determined via confocal microscopy (S Neox, Sensofar, Terrassa, Spain).

Data were analyzed using the software package SurfaceLab 7.2 (IONTOF GmbH, Münster, Germany). Present overlay images were created using RGB function of SurfaceLab with binning 4 pixels and shift correction. For visualized depth profiles 4 layers were bound in *z*-direction while overlayers were created with RGB function and shift correction.

Supporting Information

Supporting Information is available from the Wiley Online Library or from the author.

Acknowledgements

Conflict of Interest

The authors declare no conflict of interest.

Author Contributions

C.K. developed the project idea. Z.D. designed the experiments. T.O. performed cross sections experiments for SIMS, and M.R. support in SIMS analysis. Z.D., C.K., T.O., and M.R. interpreted SIMS analysis. J.K.E. conducted the simulation. Z.D., C.K., J.K.E., C.H., and T.O. interpreted the simulation result. Z.D. performed TEM sample preparation and characterization. Y.T supported the in situ experiments and Y.D. supported in the ACOM acquisition. Z.D. and C.K. interpreted TEM analysis. C.K. and J.J. supervised the project. Z.D., Y.T., G.M., and C.K. wrote the manuscript. All authors discussed the results and contributed to the preparation and revision of the manuscript.

Data Availability Statement

The data that support the findings of this study are openly available in Radar4KIT at https://doi.org/10.35097/1575, reference number 1575.

Keywords

[1] C. A. Beevers, M. A. S. Ross, *Z. Kristallogr. – Cryst. Mater.* **1937**, *97*, 59.

[2] W. L. Bragg, C. Gottfried, J. West, *Z. Kristallogr. – Cryst. Mater.* **1931**, *77*, 255.

[3] P. Pujar, B. Gupta, P. Sengupta, D. Gupta, S. Mandal, *J. Eur. Ceram. Soc.* **2019**, *39*, 4473.

[4] J. L. Sudworth, *J. Power Sources* **1994**, *51*, 105.

[5] A. Banerjee, X. Wang, C. Fang, E. A. Wu, Y. S. Meng, *Chem. Rev.* **2020**, *120*, 6878.

[6] D. Cao, X. Sun, Q. Li, A. Natan, P. Xiang, H. Zhu, *Matter* **2020**, *3*, 57.

[7] H. Liu, X.-B. Cheng, J.-Q. Huang, H. Yuan, Y. Lu, C. Yan, G.-L. Zhu, R. Xu, C.-Z. Zhao, L.-P. Hou, C. He, S. Kaskel, Q. Zhang, *ACS Energy Lett.* **2020**, *5*, 833.

[8] X. Liu, R. Garcia-Mendez, A. R. Lupini, Y. Cheng, Z. D. Hood, F. Han, A. Sharafi, J. C. Idrobo, N. J. Dudney, C. Wang, C. Ma, J. Sakamoto, M. Chi, *Nat. Mater.* **2021**, *20*, 1485.

[9] H. Gao, X. Ai, H. Wang, W. Li, P. Wei, Y. Cheng, S. Gui, H. Yang, Y. Yang, M.-S. Wang, *Nat. Commun.* **2022**, *13*, 5050.

[10] Y. Chang, W. Lu, J. Guénolé, L. T. Stephenson, A. Szczpaniak, P. Kontis, A. K. Ackerman, F. F. Dear, I. Mouton, X. Zhong, S. Zhang, D. Dye, C. H. Liebscher, D. Ponge, S. Korte-Kerzel, D. Raabe, B. Gault, *Nat. Commun.* **2019**, *10*, 942.

**ADVANCED
SCIENCE NEWS**

www.advancedsciencenews.com

**ADVANCED
ENERGY
MATERIALS**

www.advenergymat.de

[11] J. Yue, Y.-G. Guo, *Nat. Energy* **2019**, *4*, 174.

[12] J. A. Dawson, P. Canepa, M. J. Clarke, T. Famprikis, D. Ghosh, M. S. Islam, *Chem. Mater.* **2019**, *31*, 5296.

[13] S. Yu, D. J. Siegel, *ACS Appl. Mater. Interfaces* **2018**, *10*, 38151.

[14] L. Cheng, W. Chen, M. Kunz, K. Persson, N. Tamura, G. Chen, M. Doeff, *ACS Appl. Mater. Interfaces* **2015**, *7*, 2073.

[15] J. A. Dawson, P. Canepa, T. Famprikis, C. Masquelier, M. S. Islam, *J. Am. Chem. Soc.* **2018**, *140*, 362.

[16] Y. Wang, G. Li, K. Shen, E. Tian, *Mater. Res. Express* **2021**, *8*, 025508.

[17] Z. Zou, N. Ma, A. Wang, Y. Ran, T. Song, B. He, A. Ye, P. Mi, L. Zhang, H. Zhou, Y. Jiao, J. Liu, D. Wang, Y. Li, M. Avdeev, S. Shi, *Adv. Funct. Mater.* **2021**, *31*,

[18] T. Ortmann, S. Burkhardt, J. K. Eckhardt, T. Fuchs, Z. Ding, J. Sann, M. Rohnke, Q. Ma, F. Tietz, D. Fattakhova-Rohlfing, C. Kübel, O. Guillon, C. Heiliger, J. Janek, *Adv. Energy Mater.* **2022**, *13*.

[19] S. Wenzel, T. Leichtweiss, D. A. Weber, J. Sann, W. G. Zeier, J. Janek, *ACS Appl. Mater. Interfaces* **2016**, *8*, 28216.

[20] M.-C. Bay, M. Wang, R. Grissa, M. V. F. Heinz, J. Sakamoto, C. Battaglia, *Adv. Energy Mater.* **2020**, *10*, 1902899.

[21] J. M. Aceves, B. G. Cooksley, A. R. West, *J. Electroanal. Chem. Interfacial Electrochem.* **1978**, *90*, 295.

[22] R. O. Ansell, A. Gilmour, R. J. Cole, *J. Electroanal. Chem. Interfacial Electrochem.* **1988**, *244*, 123.

[23] N. Jiang, D. Su, J. C. H. Spence, S. Zhou, J. Qiu, *J. Mater. Res.* **2011**, *23*, 2467.

[24] T. B. Tang, M. M. Chaudhri, *J. Mater. Sci.* **1982**, *17*, 157.

[25] J.-O. Bovin, *Naturwissenschaften* **1984**, *71*, 263.

[26] R. o. Ansell, *J. Mater. Sci.* **1986**, *21*, 365.

[27] F. Tietz, J. Koepke, W. Urland, *J. Cryst. Growth* **1992**, *118*, 314.

[28] L. C. De Jonghe, L. Feldman, A. Beuchele, *J. Mater. Sci.* **1981**, *16*, 780.

[29] T. Krauskopf, F. H. Richter, W. G. Zeier, J. Janek, *Chem. Rev.* **2020**, *120*, 7745.

[30] H.-K. Tian, Z. Liu, Y. Ji, L.-Q. Chen, Y. Qi, *Chem. Mater.* **2019**, *31*, 7351.

[31] Y. Dong, Z. Zhang, A. Alvarez, I.-W. Chen, *Acta Mater.* **2020**, *199*, 264.

[32] L. Geng, Q. Liu, J. Chen, P. Jia, H. Ye, J. Yan, L. Zhang, Y. Tang, J. Huang, *Nano Res.* **2021**, *15*, 2650.

[33] Q. Liu, L. Zhang, H. Sun, L. Geng, Y. Li, Y. Tang, P. Jia, Z. Wang, Q. Dai, T. Shen, Y. Tang, T. Zhu, J. Huang, *ACS Energy Lett.* **2020**, *5*, 2546.

[34] K. Li, Y. Yang, X. Zhang, S. Liang, *J. Mater. Sci.* **2020**, *55*, 8435.

[35] C. Zhu, T. Fuchs, S. A. L. Weber, F. H. Richter, G. Glasser, F. Weber, H.-J. Butt, J. Janek, R. Berger, *Nat. Commun.* **2023**, *14*, 1300.

[36] R. Raj, J. Wolfenstine, *J. Power Sources* **2017**, *343*, 119.

[37] F. Han, A. S. Westover, J. Yue, X. Fan, F. Wang, M. Chi, D. N. Leonard, N. J. Dudney, H. Wang, C. Wang, *Nat. Energy* **2019**, *4*, 187.

[38] L. C. De Jonghe, *J. Electrochem. Soc.* **1982**, *129*, 752.

[39] J. K. Eckhardt, S. Burkhardt, J. Zahnow, M. T. Elm, J. Janek, P. J. Klar, C. Heiliger, *J. Electrochem. Soc.* **2021**, *168*, 090516.

[40] J. K. Eckhardt, P. J. Klar, J. Janek, C. Heiliger, *ACS Appl. Mater. Interfaces* **2022**, *14*, 35545.

[41] J. K. Eckhardt, T. Fuchs, S. Burkhardt, P. J. Klar, J. Janek, C. Heiliger, *ACS Appl. Mater. Interfaces* **2022**, *14*, 42757.

[42] M. S. Whittingham, R. A. Huggins, *J. Chem. Phys.* **2003**, *54*, 414.

2302322 (14 of 14)